Coupling of light and mechanics in a photonic crystal waveguide

J.-B. Béguin[a,1,2], Z. Qin[a,b,1], X. Luan[a], and H. J. Kimble[a,3]

[a]Norman Bridge Laboratory of Physics MC12-33, California Institute of Technology, Pasadena, CA 91125; and [b]State Key Laboratory of Quantum Optics and Quantum Optics Devices, Institute of Opto-Electronics, Shanxi University, Taiyuan 030006, China

Contributed by H. J. Kimble, September 30, 2020 (sent for review July 15, 2020; reviewed by Tobias J. Kippenberg and Dalziel Wilson)

Observations of thermally driven transverse vibration of a photonic crystal waveguide (PCW) are reported. The PCW consists of two parallel nanobeams whose width is modulated symmetrically with a spatial period of 370 nm about a 240-nm vacuum gap between the beams. The resulting dielectric structure has a band gap (i.e., a photonic crystal stop band) with band edges in the near infrared that provide a regime for transduction of nanobeam motion to phase and amplitude modulation of an optical guided mode. This regime is in contrast to more conventional optomechanical coupling by way of moving end mirrors in resonant optical cavities. Models are developed and validated for this optomechanical mechanism in a PCW for probe frequencies far from and near to the dielectric band edge (i.e., stop band edge). The large optomechanical coupling strength predicted should make possible measurements with an imprecision below that at the standard quantum limit and well into the backaction-dominated regime. Since our PCW has been designed for near-field atom trapping, this research provides a foundation for evaluating possible deleterious effects of thermal motion on optical atomic traps near the surfaces of PCWs. Longer-term goals are to achieve strong atom-mediated links between individual phonons of vibration and single photons propagating in the guided modes (GMs) of the PCW, thereby enabling optomechanics at the quantum level with atoms, photons, and phonons. The experiments and models reported here provide a basis for assessing such goals.

nanophotonics | optomechanics | quantum optics | atomic physics

Recent decades have seen tremendous advances in the ability to prepare and control the quantum states of atoms, atom-like systems in the solid state, and optical fields in cavities and free space. However, the integration of these diverse elements to achieve efficient quantum information processing still faces diverse challenges, including the wide range of highly dissimilar physical systems (e.g., atoms, ions, solid-state defects, quantum dots) that could be utilized to realize heterogeneous systems for quantum logic, memory, and long-range coupling. Each of these systems has unique advantages, but they are disparate in their frequencies, their spatial modes, and the fields to which they couple. For example, the electronic degrees of freedom in atoms and atom-like defects typically respond at optical frequencies, while their spin degrees of freedom, which are suitable for long-term storage of quantum states, respond to microwave or radio frequencies. On the other hand, the transmission of quantum information over long distances at room temperature requires the use of telecom-band photons in single-mode optical fibers.

Beginning with the pioneering work in refs. 1 and 2, mechanical systems have now been recognized as broadly applicable means for overcoming these disparities and transferring quantum states between different quantum degrees of freedom (3–6). This is because mechanical systems (7) can be engineered to couple efficiently and coherently to many different systems and can possess very low damping, particularly when operated at cryogenic temperatures. To date, quantum effects have been observed in mechanical systems coupled to superconducting qubits (via piezoelectric coupling) (8), optical photons (9–14), and microwave photons (15, 16). Efficient coupling has also been demonstrated between mechanical oscillators and spins in various solid-state systems, although to date the mechanical components of these devices have operated in the classical regime (17–23).

In this article we describe nascent efforts to utilize strong coupling of atoms, photons, and phonons in nanophotonic photonic crystal waveguides (PCWs) to create a different generation of capabilities for quantum science and technology. Our long-term goal is to use optomechanical systems operating in the quantum regime to realize controllable, coherent coupling between isolated, few-state quantum systems. In our case, the system will consist of atoms trapped along a PCW that interact strongly with photons propagating in the guided modes (GMs) of the PCW (24). The mechanical structure of the PCW in turn supports phonons in its various eigenmodes of motion. While much has been achieved in theory and experiment for strong coupling of atoms and photons in nanophotonics, much less has been achieved (or even investigated) for the optical coupling of motion and light in the quantum regime for devices such as described in refs. 24 and 25.

A longstanding challenge for this work is to achieve the integration of ultracold atoms with nanophotonic devices. If this

Significance

High-Q mechanical modes of transverse oscillation at a few megahertz are characterized for a photonic crystal waveguide (PCW) consisting of parallel dielectric nanobeams. The transduction of thermally excited motion of 33 pm at 300 K results in phase modulation with high signal-to-noise ratio for light propagating in a guided mode of the PCW. Numerical modeling gives good agreement with experiment. With these measurements in hand, the system is assessed for possible applications in quantum information science and technology involving strong coupling of single phonons of vibration to single atoms and photons trapped within the PCW.

Author contributions: J.-B.B., Z.Q., and H.J.K. designed research; J.-B.B., Z.Q., X.L., and H.J.K. performed research; J.-B.B. and Z.Q. contributed new analytic tools; J.-B.B., Z.Q., X.L., and H.J.K. analyzed data; and J.-B.B., Z.Q., X.L., and H.J.K. wrote the paper.

Reviewers: T.J.K., École Polytechnique Fédérale de Lausanne; and D.W., University of Arizona.

The authors declare no competing interest.

[1]J.-B.B. and Z.Q. contributed equally to this work.

[2]Present address: Niels Bohr Institute, University of Copenhagen, 2100 Copenhagen, Denmark.

[3]To whom correspondence may be addressed. Email: hjkimble@caltech.edu.

This article contains supporting information online at https://www.pnas.org/lookup/suppl/doi:10.1073/pnas.2014851117/-/DCSupplemental.

First published November 9, 2020.

challenge were overcome, quantum motion could be harnessed to investigate enhanced nonlinear atom–light interactions with single and multiple atoms. Additional quantum phases (31), different mechanisms for controlling atoms near dielectric objects (32), and strong atom–photon–phonon coupling (6) could be realized in the laboratory. Although difficult, this approach potentially benefits from several advantages when compared to conventional optomechanics, including 1) the extreme region of parameter space that atomic systems occupy (such as low mass and high mechanical Q factors), 2) the exquisite level of control and configurability of atomic systems, and 3) the preexisting quantum functionality of atoms, including internal states with very long coherence times.

Of course, many spectacular advances of atomic physics already build upon these features (33–35). On one hand, experiments with linear arrays of trapped ions achieve coherent control over phonons interacting with the ions' internal states as pseudospins. Goals that are very challenging for quantum optomechanics with nano- and microscopic masses, such as phonon-mediated entanglement of remote oscillators and single-phonon strong coupling, are routinely implemented with trapped ions. On the other hand, cavity quantum electrodynamics (QED) with neutral atoms produces strong interactions between single photons and the internal states of single atoms or ensembles, leading to demonstrations of state mapping and atom–photon entanglement (36).

What is missing thus far, and what motivates the initial steps described here, is a strong atom-mediated link between individual photons and phonons, to enable optomechanics at the quantum level. Initial steps described here include 1) observation and characterization of the low-frequency, mechanical eigenmodes of an alligator photonic crystal waveguide (APCW) (26–29) and 2) the development of theoretical models that are validated in the nontraditional regime in which our system works (37, 38), namely, well-localized mechanical modes, but nonlocalized propagating photons both far from and near to the band edges of PCWs.

The Alligator Photonic Crystal Waveguide

Fig. 1 provides an overview of the APCW utilized in our experiments with details related to device fabrication and characterization provided in refs. 26–29. The photonic crystal itself is formed by external sinusoidal modulation of two parallel nanobeams made of stoichiometric silicon nitride to create a photonic bandgap for transverse electric (TE) modes with polarization predominantly along y in Fig. 1*A*. The TE band edges have frequencies near the D1 and D2 transitions in atomic cesium (Cs). Calculated and measured dispersion relations for such devices are presented in ref. 27, where good quantitative agreement is found. Here, we focus on coupling of light and motion for TE modes of the APCW. Transverse magnetic (TM) modes of the APCW near the TE band edges resemble the guided modes of an unstructured waveguide.

As shown by the SEM image in Fig. 1*B*, the APCW is connected to single-beam waveguides on both ends and thereby freely suspended in the center of a 2-mm-wide window in a silicon chip. Well beyond the field of view in Fig. 1*B*, a series of tethers are attached transversely to the single-beam waveguides along $\pm y$ to anchor the waveguides to two side rails that run parallel to the x axis of the device to provide thermal anchoring and mechanical support, with the coordinate system defined in Fig. 1*A*. Important for our current investigation, the single-beam waveguides and the APCW itself are under tensile stress with $\sigma \simeq 800\,\mathrm{MPa}$.

Light is coupled into and out of TE guided modes of the APCW by a free-space coupling scheme that eliminates optical fibers within the vacuum envelope (39, 40). An example of a reflection spectrum $R(\nu)$ is given Fig. 1*C*, which is acquired by way of light launched from and recollected by the microscope objective O1 shown in Fig. 1*D*. Objectives O1 and O2 are mode matched to the fields to/from the terminating ends of the waveguide, resulting in overall throughput efficiency $\simeq 0.50$ from input objective O1 through the device with the APCW to output objective O2 for the experiments described here. The silicon chip itself contains a set of APCWs and is affixed to a small glass optical

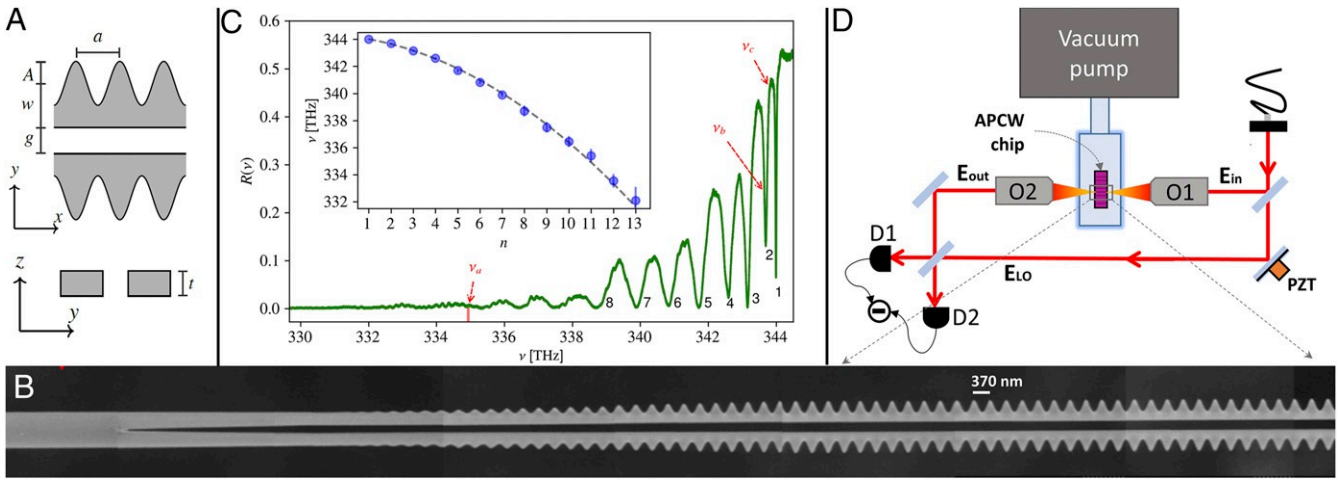

Fig. 1. Details of the APCW and the setup for our experiments (26–29). (*A*) Drawing giving the dimensions of the various components of the APCW in gray. The unit cell spacing $a = 370\,\mathrm{nm}$, the vacuum gap $g = 238\,\mathrm{nm}$, and the silicon nitride thickness $t = 200\,\mathrm{nm}$. The outer beams have modulation amplitude $A = 120\,\mathrm{nm}$ and width $w = 280\,\mathrm{nm}$. (*B*) An SEM image of the left half of the APCW showing (from left to right) a single unstructured rectangular waveguide that splits at a Y junction into two parallel waveguides each of which is gradually modulated in width to finally match the A, w values of the APCW itself which extends 150 unit cells to the right along x before tapering to a second Y junction and a uniform rectangular beam. The entire structure is suspended in vacuum by transverse tethers connected to supporting side rails as shown in ref. 26, figure 3 and ref. 30, figure 1.9. (*C*) Reflection spectrum $R(\nu)$ for the APCW displays a series of low-finesse cavity-like resonances for reflections from the input tapers and APCW near the dielectric band edge at 344 THz. *Inset* plots frequencies ν_n for successive cavity resonances $n = 1, 2, \ldots$ near the dielectric band edge. (*D*) Simplified diagram for measurements of mechanical modes of the APCW by way of transmission spectra $T(\nu)$ either by direct detection of beam $E_{\mathrm{out}}(\nu)$ alone at photodetector D_1 or D_2 or via balanced homodyne detection of the signal beam $E_{\mathrm{out}}(\nu)$ combined with the local oscillator beam $E_{\mathrm{LO}}(\nu)$ at photodetectors D_1 and D_2.

table inside a fused silica vacuum cell by way of silicate bonding (39, 40).

Observations of Modulation Spectra

With reference to Fig. 1*D*, we have recorded spectra $\Phi(\nu, f, \theta)$ for the difference of photocurrents from detectors D_1, D_2 for light transmitted through an APCW for various probe frequencies ν below the frequency $\nu_{BE} \simeq 344\,\mathrm{THz}$ of the dielectric band edge. Here we employ a balanced homodyne scheme with E_{in} and E_{LO} having identical optical frequency ν and each absent radio-frequency modulation f save that from propagation in the APCW. With free-space coupling to guided modes of the APCW, homodyne fringe visibility up to ~ 0.95 is obtained.

Measurement results for $\Phi(\nu, f, \theta)$ are displayed in Figs. 2 and 3 for three optical frequencies $\{\nu_a, \nu_b, \nu_c\} = \{334.96, 343.64, 343.78\,\mathrm{THz}\}$ (i.e., wavelengths $\{895.00, 872.40, 872.04\,\mathrm{nm}\}$) moving from far below to near the dielectric band edge, as marked by red arrows in Fig. 1*C*. The spectra display a series of narrow peaks and are of increasing complexity as the band edge is approached. All spectra are taken for a weak probe beam $E_{out}(\nu)$ with power $P_{out} \sim 10\,\mu\mathrm{W}$, while $P_{LO} \simeq 0.5\,\mathrm{mW}$. The phase offset θ between E_{in} and E_{LO} is set to maximize the observed spectral peaks whose frequencies f exhibit only small shifts with changes in P_{out}, as illustrated in *SI Appendix*, Fig. S1. In vacuum ($\sim 1 \times 10^{-10}$ torr) and at room temperature, the quality factor for the lowest peak at $f_1 \simeq 2.4\,\mathrm{MHz}$ is $Q \simeq 1 \times 10^5$.

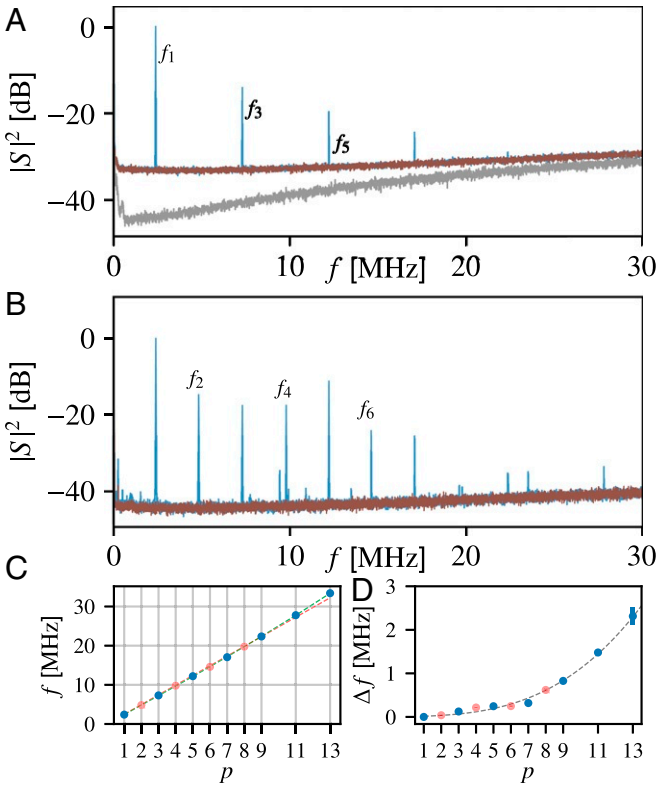

Fig. 2. (*A* and *B*) Measured vibration spectra with an electrical spectrum analyzer (bandwidth 10 kHz) at wavelength 895.00 nm (*A*) and 872.40 nm (*B*), respectively. The detector output with blocked and unblocked light probe E_{out} is shown in the brown and blue traces, respectively. The detector output with no light (all light sources blocked) is shown in gray in *A* (photodetector bandwidth 4 MHz in *A* and 45 MHz in *B*). *C* plots the frequencies f_p of odd quasi-harmonics peaks (blue dots) and even quasi-harmonics peaks (red dots) of f_1. Linear fit (dashed red curve) and complete fit (dashed green curve) of $\tilde{f}_p$ are also shown. *D* plots the measured frequency difference Δf (blue and red dots) and theoretical fit $\Delta\tilde{f}$ (dashed gray curve).

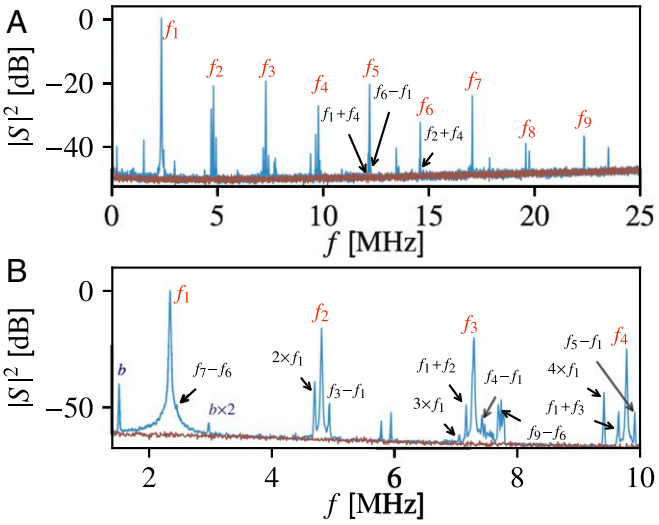

Fig. 3. (*A* and *B*) Measured vibration spectra near the band edge at 872.04 nm (ν_c) with spans of 25 MHz (*A*) and 10 MHz (*B*). As in Fig. 2*B*, the detector output with blocked and unblocked light probe E_{out} is shown in the brown and blue traces, respectively. Except for the dominant peaks appearing in Fig. 2 (i.e., approximate integer harmonics of f_1 labeled in red), sums and differences of the dominant quasi-harmonics frequency components are also observed. Peak labeled as *b* is due to unbalanced input laser light noise (photodetector bandwidth 45 MHz).

An important feature of the spectra in Fig. 2*A* is that peaks beyond f_1 occur at frequencies that are approximately odd harmonics of f_1, with $f_j \simeq j \times f_1$ for $j = 1, 3, 5, \ldots$. By contrast in Fig. 2*B*, the largest peaks double in number with now the presence of even harmonics of the fundamental frequency f_1 in addition to the odd harmonics from Fig. 2*A*. As shown in Fig. 2*C*, the dispersion relation is approximately linear with frequencies $f_p \simeq p \times f_1$, where $p = 1, 2, 3, \ldots$.

Further understanding emerges if we consider higher accuracy for the frequencies f_p and examine the measured frequency differences $\Delta f = \{f_p - p f_1\}$ as in Fig. 2*D*. Also plotted as the dashed line is the theoretical prediction for the mechanical frequency differences $\Delta\tilde{f} = \{\tilde{f}_p - p\tilde{f}_1\}$ of a long, narrow, and thin beam, which is supported at hinged ends. For this model, the mechanical resonances are (41)

$$\tilde{f}_p = \frac{p^2\pi}{2L^2}\sqrt{\frac{EI}{\rho A} + \frac{\sigma L^2}{\rho\pi^2 p^2}}, \qquad [1]$$

where p is the integer mode index, E the Young's modulus, I the moment of inertia, A the cross-sectional beam area, L the beam length, ρ the mass density, and σ the beam stress.

Our APCW and connecting nanobeams are fabricated from Si_3N_4 with high-tensile stress $\sigma \simeq 800\,\mathrm{MPa}$ (26, 28). Together with the largely one-dimensional (1D) geometry of the APCW (large aspect ratio of transverse to longitudinal dimension), the contribution of the bending term in Eq. **1** can be neglected for the lowest-order modes such that $\tilde{f}_p \simeq (p/2L)\sqrt{\sigma/\rho}$, giving rise to a close approximation of the linear dispersion of a tensioned string as in Fig. 2*C*. However, higher-order modes have a clear quadratic contribution from the bending term that is evident in Fig. 2*D*.

In terms of absolute agreement between measured and predicted frequencies for the spectra in Fig. 2, from Eq. **1** we calculate a fundamental frequency $\tilde{f}_1 = 2.37 \pm 0.3\,\mathrm{MHz}$ from the total length $L = 180 \times a + 2 \times 20\,\mu\mathrm{m} = 107 \pm 10\,\mu\mathrm{m}$ with the unit cell spacing $a = 0.37\,\mu\mathrm{m}$, the manufacturer's quoted tensile stress $\sigma = 800 \pm 50\,\mathrm{MPa}$, and the mass density for (stochiometric)

silicon nitride produced by low-pressure chemical vapor deposition (LPCVD) (42), $\rho_{Si_3N_4} = 3{,}180\,\mathrm{kg{\cdot}m^{-3}}$. For the length L, we consider the 150 unit cells of the actual PCW region, plus the 30 tapered cells on each end, and finally the length from the beginning of the Y-split junction which separates the two corrugated beams. The devices are designed for small stress relaxation from that of the original Si_3N_4 on a silicon chip (28). The predicted $\tilde{f}_1$ is close to the measured frequency $f_1 = 2.3844\,\mathrm{MHz}$.

While the frequencies of the largest peaks in Fig. 2 are well described by Eq. **1**, the complexity of the spectra increases as the band edge is approached with the appearance of many small satellite peaks as in Fig. 3 for $\nu_c = 343.78\,\mathrm{THz}$ (i.e., wavelength $\lambda_c = 872.04\,\mathrm{nm}$).

After labeling for clarity the dominant even and odd quasi-harmonics that also appear in Fig. 2, we clearly observe a secondary series of integer harmonics in Fig. 3, such as the second, third, and fourth harmonics of the lowest-frequency f_1. The majority of the remaining peaks have frequencies which coincide with sums and differences of the main quasi-harmonics frequency components f_p. Nonlinear transduction of thermomechanical fluctuations has been observed previously, for example in ref. 43 with a sliced photonic crystal nanobeam. A recent study (44) thoroughly investigated its impact on limiting noise figures for quantum optomechanics. Other peaks (e.g., at 1.5 MHz) originate from unbalanced input laser light noise.

Mechanical Modes of the APCW

From measurements as in Figs. 2 and 3 in hand and some understanding of the dispersion relation for the observed mechanical modes of the APCW, we turn next to more detailed characterization by way of numerical simulation. Principal goals are 1) to determine the mechanical eigenfunctions (and not just eigenfrequencies) associated with the observed modulation spectra and 2) to investigate the transduction mechanisms that convert mechanical motion of the various eigenfunctions to modulation of our probe beam. Beyond numerics to find the mechanical eigenmodes, we present simple models to describe the transduction of mechanical motion to light modulation for various regimes far from and near to a band edge of the APCW. Quantitative numerical evaluation of the optomechanical coupling rate G_ν and eigenmodes for the full APCW structure are presented in *Numerical Evaluation of the Optomechanical Coupling Rate G_ν*.

Fig. 4 shows the fundamental mechanical modes of a small APCW structure obtained via numerical solution of the elastic equations. For clarity, we illustrate with a reduced geometry due to the large aspect ratio of our structure. Fig. 4 *A–D* represents the three-dimensional (3D) deformed geometry as prescribed by the displacement vector field associated to each of the mechanical eigenmodes, with an arbitrary choice of mechanical energy. The displacement u normalized to its maximum value u_{max} is indicated by the colormap. Fig. 4*E* displays a higher-order antisymmetric mode with $f_3^{y,A} \sim 3f_1^{y,A}$ in the *x-y* plane for a longer structure.

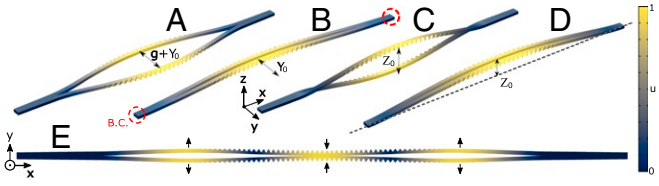

Fig. 4. Mechanical modes of the APCW structure illustrated with a reduced geometry. Four types of eigenmodes are shown: (*A*) Y_1^A, (*B*) Y_1^S, (*C*) Z_1^A, and (*D*) Z_1^S, where the total number of APCW unit cells is $N = 10$, the total number of taper cells $N_t = 15$, and the length of a single Y-split junction $L_Y = 6\,\mu\mathrm{m}$. *E* shows a higher-order mode Y_3^A for a longer structure with $N = 30$, $N_t = 30$, $L_Y = 12\,\mu\mathrm{m}$. B.C. means two end-clamped boundary conditions. Arbitrary displacement amplitude scales were chosen for illustration purposes (main text).

The design of the relatively long Y junction arises from the need for efficient (i.e., adiabatic) conversion of the light guided from the single waveguide into the mode of the double-beam photonic crystal. While it does not represent a sharp boundary for the mechanics (please refer to refs. 28 and 29 for details of the full suspended structure with anchoring tethers), it does impose a symmetric termination geometry for both patterned beams. For the choice of effective two end-clamped boundary conditions, the four types of eigenmodes consist of two pairs of symmetric S and antisymmetric A oscillation, one pair with motion predominantly along y, which we denote by Y_p^A, Y_p^S, and the other with motion mainly along z, denoted by Z_p^A, Z_p^S and labeled by the mode number $p = 1, 2, 3, \ldots$. For the actual full APCW structure, the eigenfrequencies for the fundamental $p = 1$ modes are in the ratio $f_1^{y,A}, f_1^{y,S} f_1^{z,A}, f_1^{z,S} = 1, 0.77, 0.98, 0.74$.

While the modes in Fig. 4 correspond to the mode families with lowest eigenfrequencies, at higher frequency other types of beam motion with mixed $y-z$ displacements appear. Also, as discussed in *Conclusion and Outlook*, the APCW is a 1D phononic crystal. The eigenmodes shown in Fig. 4 correspond roughly to those of two weakly coupled nanobeam oscillators. They are representative of the flexural modes studied in other works such as tuning fork nanomechanical resonators (45) and photonic crystal optomechanical zipper cavities (46), whose geometries have a more apparent doubly clamped boundary condition. Regarding the accuracy of the choice of boundary condition, we note that the mechanical properties of the differential modes are little impacted by the length of the single beam beyond the merging point of the junction.

Mapping Motion to Optical Modulation

Optical Frequencies Far from a Band Edge. A simple model for the transduction of motion of the APCW nanobeams into optical modulation explains some of the key observations from the previous sections. First of all, for a fixed GM frequency ω input to the APCW, each mechanical eigenmode adiabatically modifies the band structure of the APCW and thereby the optical dispersion relation $k_x(\omega)$ for GM propagation along x with frequency ω relative to the case with no displacement from equilibrium. In our original designs of the APCW, we undertook extensive numerical simulations of the band structure for variations of all of the dimensions shown in Fig. 1*A* (27–29). Guided by these earlier investigations, we deduce that the largest change in band structure with low-frequency motion as in Fig. 4 arises from variation of the gap width g from displacements $\pm\delta y/2$ for the antisymmetric eigenmode Y_p^A illustrated in Fig. 4*A*.

As suggested by Eq. **1**, we then consider a 1D string model with $Y_p^A(x)$ describing y displacement at each point along x, namely $Y_p^A(x) = Y_{0,p}\sin(\beta_p x)$, with maximum y displacement $Y_{0,p}$. Here, β_p is the mechanical wave vector with $Y_p^A(x)$ subject to boundary conditions, which in the simplest case are $Y_p^A(x=0) = 0 = Y_p^A(L)$ with then eigenvalues $\beta_p = p\pi/L$ for $p = 1, 2, 3, \ldots$. Again, $Y_p^A(x)$ denotes the mechanical eigenmode in Fig. 4*A* and represents antisymmetric y displacements of each nanobeam, with one beam of the APCW having displacement from equilibrium $\pm\delta y = \pm Y_0/2$ and the opposing beam with phase-coherent displacement $\mp\delta y = \mp Y_0/2$, leading to a cyclic variation of the total gap width $g \to g + Y_0 \to g \to g - Y_0 \to g$ as described by $Y_p^A(x)$ along the x axis of the APCW. For small y displacements and fixed frequency ω far from the band edge, we can then expand the dispersion relation to find $k_x(\omega, y) \simeq k_x(\omega, 0) + \delta k_x(\omega, y)$, where $\delta k_x(\omega, y) = \xi(\omega) \times y$, with $\xi(\omega) = (\frac{dk_x(\omega)}{dy})$.

Since y displacements vary along x as described by the particular mechanical eigenmode $Y_p^A(x)$, δk_x will also vary along x. The differential phase shift due to a mechanical eigenmode for propagation of an optical GM from input to output of the APCW is then given by (in our simple model) $\Phi_p(L) = \int_0^L \delta k_x(\omega, Y_p^A(x))\,dx = \int_0^L \xi(\omega)\, Y_p^A(x)\,dx = 2L\xi(\omega)\, Y_0/p\pi$ for p odd and $\Phi_p(L) = 0$ for p even. Here, $\Phi_p(L)$ is the differential phase shift between optical propagation through the APCW with and without mechanical motion (i.e., $Y_{0,p} \neq 0$ and $Y_{0,p} = 0$).

When driven by thermal Langevin forces, the mechanical mode $Y_p^A(x)$ oscillates principally along y at frequency $f_p^{y,A}$ with rms amplitude $\langle Y_{0,p}^2 \rangle^{1/2}$, where $\langle Y_{0,1}^2 \rangle^{1/2} \simeq 64\,\mathrm{pm}$ as calculated in *SI Appendix*. For small, thermally driven phase shifts, $\Phi_p(L)$ likewise oscillates predominantly at $f_p^{y,A}$ with rms amplitude linearly proportion to y displacement, $\langle \Phi_p^2 \rangle^{1/2} \propto \langle Y_{0,p}^2 \rangle^{1/2}$. Far from a band edge, both Φ_p and $Y_{0,p}$ should be Gaussian random variables, with, for example, probability density $P(\Phi_p) = e^{-\Phi_p^2/2\sigma_p^2}/\sqrt{2\sigma_p}$.

Measurements of Phase and Amplitude Modulation. Overall, our simple model describes mechanical motion via eigenmodes $Y_p^A(x)$ that modifies the dispersion relation for an optical GM, which in turn leads to nonzero phase modulation Φ_p at frequency f_p for p odd eigenmodes and zero phase modulation for p even modes, precisely as observed in Fig. 2*A* far from the band edge. Here we present measurements to substantiate further this model.

With reference to Fig. 1*D*, the balanced homodyne detector enables measurement of an arbitrary phase quadrature by offset of the relative phase θ between the probe output field E_{out} and the local oscillator field E_{LO} with θ set by adjusting the voltage of the piezoelectric mirror mount (PZT) shown in Fig. 1*D*. Phase or amplitude modulation of the probe field is then unambiguously identified by offset $\theta = \pi/2$ for PM or $\theta = 0$ for AM. By calibrating the low-frequency ($f \simeq 80\,\mathrm{Hz}$) fringe amplitude for the difference current $\Delta i(t)$ of the balanced homodyne signal as a function of $\theta(t)$ and then setting $\theta = \pi/2$ (i.e., at the zero crossing of the interferometer fringe signal for highest phase sensitivity), we observe periodic variation in $\Delta i(t)$ at $f \simeq 2.384\,\mathrm{MHz}$, corresponding precisely to the lowest $p = 1$ eigenfrequency $f_1^{y,A}$ in the phase $\Phi_1(t)$ imprinted on the probe from propagation through the APCW. Fig. 5 displays an example of a single time trace for fixed $\theta = \pi/2$ clearly evidencing $\Phi_1(t)$ both for broad bandwidth detection and for processing with a digital bandpass filter centered at $f_1^{y,A}$ with $\pm 100\,\mathrm{kHz}$ bandpass.

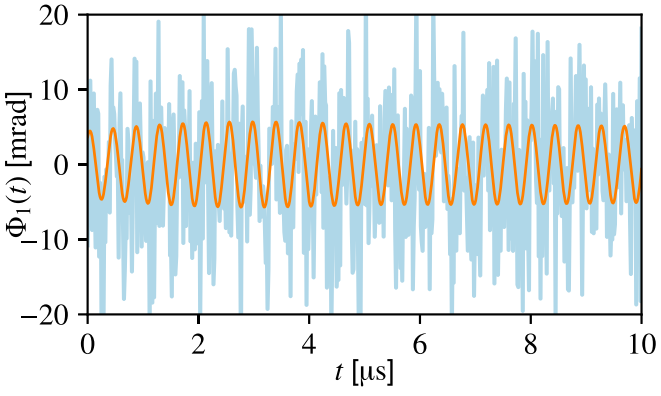

Fig. 5. Single-shot relative phase between probe signal and local oscillator field extracted from the balanced homodyne photocurrent. (Blue) The data are recorded on a digital oscilloscope with a 62.5-MHz sampling rate. (Orange) Bandpass filtered data with high-cut and low-cut frequencies at $f_1 \pm 100$ kHz. The optical wavelength of the probe is 895.00 nm.

Over a range of probe powers (*SI Appendix*, Fig. S2) and frequencies far from the band edge (*SI Appendix*, Fig. S3), the typical observed rms amplitude of the detected phase modulation at $f_1^{y,A}$ is $(4.5 \pm 2.0) \times 10^{-3}$ rad. This measured modulation for $\Phi_1(t)$ should be compared to the value predicted from our simple model. The thermally driven y amplitude $Y_{0,p=1}$ is calculated in *SI Appendix* and can be combined with a transduction factor $\xi(\omega) = (\frac{dk_x(\omega)}{dy})$ inferred from band structure calculations to arrive to a predicted rms value for thermally driven phase modulation at frequency $f_1^{y,A}$ of about 4×10^{-3} rad (*SI Appendix*). In *Numerical Evaluation of the Optomechanical Coupling Rate* G_v we address the origin of disparity between measured and modeled phase modulation by way of full numerical simulation for the APCW.

Note that we observe a shift of the mechanical frequency with guided probe power, which allows an inference of the bare mechanical frequency f_1^0 in the absence of probe light. Representative data for the power-dependent shift can be found in *SI Appendix*, Fig. S1, which shows a linear decrease with probe power P of $f_1 = f_1^0 + \beta P_{\mathrm{out}}$ with $\beta = -1.31 \pm 0.02\,\mathrm{Hz \cdot \mu W^{-1}}$ and $f_1^0 = 2{,}385{,}812 \pm 10\,\mathrm{Hz}$. This shift with probe power is consistent with thermal expansion of the APCW due to absorption of probe power. Preliminary measurements of phase modulation for optical frequencies closer to the dielectric band edge are provided in *SI Appendix*, Fig. S7.

Missing Modes. There remains the question of "missing modes." If indeed the dominant spectral peaks in Fig. 2 are associated with the eigenfunctions Y_p^A, what has become of the other three sets of eigenfunctions Y_p^S, Z_p^A, Z_p^S? The answer provided by our simple model of mechanical motion modifying the dispersion relation $k_x(\omega)$ is that Y_p^A is unique in producing a large first-order change in $k_x(\omega)$ with displacement.

Fig. 4 reveals that only Y_p^A has distinct geometries for displacements $\pm\delta y$ (i.e., the two nanobeams are more separated for $+\delta y$ and less separated for $-\delta y$), leading to a much larger calculated transduction factor $\xi_{y,A}(\omega)$ for motion along y than $\xi_{z,A}(\omega)$ for motion along z. Moreover, far from the band edge, the symmetric modes Y_p^S, Z_p^S have small transduction factors $\xi_{y,S}(\omega), \xi_{zS,}(\omega)$ comparable to those for modes of a single unmodulated nanobeam of the thickness and average width of the APCW. This issue is addressed in quantitative detail in *Numerical Evaluation of the Optomechanical Coupling Rate* G_v with a full numerical simulation of optomechanical coupling for the APCW.

Optical Frequencies near a Band Edge. Near the band edge of a PCW, the mapping of mechanical motion to modulation of an optical probe, i.e., optomechanical transduction, has a qualitatively distinct origin from that in the previous section for the dispersive regime of a PCW. For a finite length PCW, there appears a series of optical resonances ν_n with $n = 1, 2, 3 \ldots$ as displayed in Fig. 1*C*. Each optical resonance arises from the condition $\delta k_x(n) = k_{\mathrm{BE}} - k_x = n\pi/L$ with $k_{\mathrm{BE}} = \pi/a$ at the band edge (27, 30). The mapping from wave vector $\delta k_x(n)$ to frequency ν_n involves a nonlinear dispersion relation $\delta k_x(\nu)$ near the band edge, which for our devices takes the form

$$\delta k_x(\nu) = \frac{2\pi}{a}\sqrt{\frac{(\nu_{\mathrm{BE2}} - \nu)(\nu_{\mathrm{BE}} - \nu)}{4\zeta^2 - (\nu_{\mathrm{BE2}} - \nu_{\mathrm{BE}})^2}}, \qquad [2]$$

where ν_{BE} (ν_{BE2}) is the lower (upper) band edge frequency, and ζ is a frequency related to the curvature of the band near

the band edge. Validation of this model by measurement and numerical simulation is provided in refs. 27 and 30.

For our current investigation, the lower-frequency ν_{BE} for which $\delta k_x = 0$ is the dielectric band edge frequency. We model how displacements of the APCW geometry for the various mechanical eigenmodes illustrated in Fig. 4 lead to variation of the parameters in Eq. **2**. Specifically, since the resonance condition involves only the effective length of the APCW (i.e., $L = (N-1)a$ with the number of unit cells $N \simeq 150$ and lattice constant $a \simeq 370\,\mathrm{nm}$), each optical resonance will be taken to have fixed $\delta k_x(n) = n/(N-1) \times k_{\mathrm{BE}}$ with then the associated optical frequency $\nu(n)$ changing due to variation of parameters in Eq. **2** driven by displacements from the mechanical eigenmodes.*

A mapping of changes in device geometry to changes in band edge frequencies is provided in ref. 29. As in the previous subsection, we seek here a qualitative description to understand the complex transduction of mechanical motion to optical modulation in a 3D PCW. Quantitative numerical calculations are described in *Numerical Evaluation of the Optomechanical Coupling Rate* G_ν.

That said, we proceed by way of table 2.1 and figure 2.13 in ref. 29 to estimate the traditional vacuum optomechanical coupling rate (7) G_ν^y for y displacements at the $n = 1$ optical resonance, ν_1, closest to the dielectric band edge at ν_{BE}. Here, $G_\nu^y(\nu_1) \equiv 2y_{\mathrm{zp}} \times \frac{d\nu(1)}{dy}$, where we consider change in resonant frequency ν_1 due to y variation of the gap width g as from the simple model in the previous section, and where the factor 2 arises for the eigenmode Y^A from the displacement $2\delta y$ for asymmetric y motion of each beam by $\pm\delta y$ and $\mp\delta y$. $y_{\mathrm{zp}} = \sqrt{\hbar/2m_{\mathrm{eff}}^y\omega_p} \simeq 14\,\mathrm{fm}$ is the zero-point amplitude along the chosen coordinate y (*SI Appendix*), with the effective mass of a 1D string $m_{\mathrm{eff}}^y = m/2$ and the mass $m \simeq 35\,\mathrm{pg}$ corresponding to that of the APCW section plus half the mass of each taper. By way of the dispersion relation Eq. **2** and ref. 29, we find that $\left|\frac{d\nu(1)}{dy}\right| \simeq 0.034\,\mathrm{THz{\cdot}nm^{-1}}$ and thus that the optomechanical coupling rate $G_\nu^y(\nu_1) \simeq 900(100)\,\mathrm{kHz}$, which is to be compared to the value found in *Numerical Evaluation of the Optomechanical Coupling Rate* G_ν for the full 3D geometry.

Numerical Evaluation of the Optomechanical Coupling Rate G_ν

In this section, we consider the full APCW structure and evaluate numerically the optomechanical coupling rate G_ν from the waveguide to the band-edge regions. We first solve for the light-field distribution propagating in the structure by launching the TE mode solution of the infinite single nanobeam waveguide section. This also gives reflection and transmission coefficients of the TE electromagnetic mode at both ends of the structure, with the reflection coefficient $R(\nu)$ shown on the right axis of Fig. 6. We neglect the small imaginary part of the refractive index for Si_3N_4 as well as losses due to fabrication imperfections. The mechanical eigenmodes are solved for the full structure (i.e., total number of unit cells for APCW $N = 150$, total number of taper cells $N_t = 30$, Y-split junction length $L_Y = 30\,\mu\mathrm{m}$) with clamped ends, taking into account a constant stress distribution which is the steady-state stress field associated to the e-beam written geometry within the sacrificial layer of Si_3N_4 with initial homogeneous in-plane stress σ.

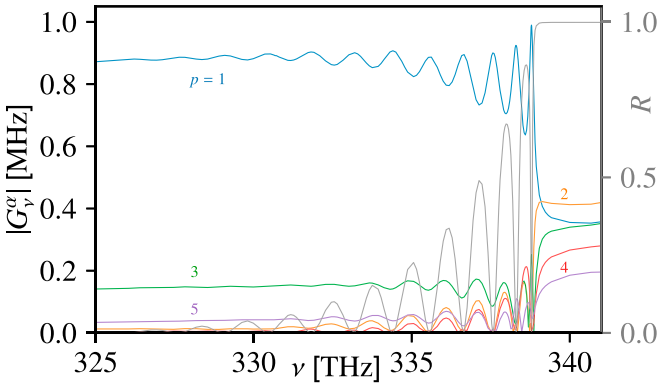

Fig. 6. Numerically calculated optomechanical coupling rate G_ν^α for eigenmodes from $p = 1$ to $p = 5$ for the family Y_p^A as functions of optical frequency ν for a TE guided mode. α is the generalized displacement coordinate defined in *SI Appendix*. Gray curve shows the reflection spectrum for the TE mode of APCW structure. Here, the number of APCW unit cells is $N = 150$, the total number of taper cells is $N_t = 30$, and the Y-split junction length is $L_Y = 30\,\mu\mathrm{m}$. (*SI Appendix*, Fig. S6 provides a zoomed-in version of this figure.)

Exploring Si_3N_4 material properties within 10% of the values provided by the wafer manufacturer, the numerically predicted mechanical frequencies are accurate to better than 0.1% with measured frequencies for $E = 250\,\mathrm{GPa}$, $\rho = 3{,}160\,\mathrm{kg{\cdot}m^{-3}}$, and $\sigma = 860\,\mathrm{MPa}$.

The exact expression for the optomechanical coupling rate G_ν due to displacement shifts of the dielectric boundaries within perturbation theory can be found in *SI Appendix* and ref. 47. It is given by the product of the mechanical zero-point motion amplitude α_{zp}, and the change in optical mode eigenfrequency due the dielectric displacement prescribed by the mechanical mode (generalized coordinate α [*SI Appendix*]), $G_\nu^\alpha = (\partial\nu/\partial\alpha)\alpha_{\mathrm{zp}}$.

The values of the coupling rate $G_\nu^\alpha(p)$ are shown in Fig. 6 for various eigenmodes p for the family Y_p^A as functions of optical frequency, where the actual eigenmode was approximated by a sine mode shape in *Mapping Motion to Optical Modulation*. While the predicted G_ν^α is largest for such a mode family, we report in *SI Appendix*, Fig. S4 the simulated values for all low-frequency modes. The calculation spans from the waveguide regime far below the TE dielectric band edge, to then approaching the band edge, and finally into the band gap itself. The value of $|G_\nu^\alpha|$ reaches up to $\sim$1.0 MHz at resonance near the band edge. This is slightly larger than predicted from the simple model in *Mapping Motion to Optical Modulation*, which ignored the finite geometry with the Y junction, tapered cells, and narrowing of the physical gap (i.e., infinite APCW).

In contrast to the strains associated with gigahertz-acoustic modes for some optomechanical systems (48) that lead to photo-elastic contributions G_{PE} comparable to those from the dielectric moving boundaries, we find that the G_{PE} contribution is negligible (by several orders of magnitude) compared to the dielectric moving boundary contribution for the long-wavelength vibrations under consideration for the APCW, for which the phonon wavelength becomes comparable to the optical wavelength. A measurement of the photo-elastic constant for Si_3N_4 can be found in ref. 49. Also note that $G_{\mathrm{PE}} \propto n^4$, with the ratio of Si_3N_4 (as here) to Si (as in ref. 48) refractive indexes $n_{Si_3N_4}/n_{Si} = 2/3$.

To validate our numerical calculations, we have reproduced published results for several nanophotonic structures, (50–52), as discussed in *SI Appendix*.

Despite their relatively large effective mass ($\simeq$20 pg; *SI Appendix*, section S1), the low-frequency mechanical modes of the APCW achieve mass-frequency products and hence

*In this regard, operation in the vicinity of an optical resonance near a band edge of a PCW is analogous to more traditional optomechanics, with, for example, Fabry–Perot cavities, for which thermally excited mechanical resonances of a cavity mirror can shift the optical resonances of a high-finesse cavity. The result on a circulating optical field can be phase or amplitude modulation, or even more exotic behavior, including parametric instability (1, 2), which we briefly discuss in *Conclusion and Outlook*.

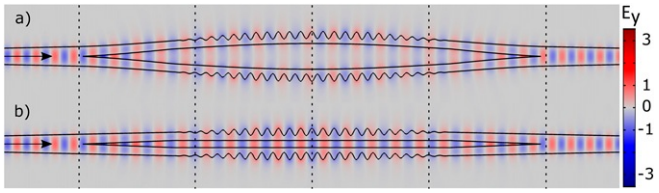

Fig. 7. (*A* and *B*) Electric-field component E_y of the TE guided mode propagating from left to right in the deformed (*A*) and unperturbed (*B*) APCW structure, both shown in the $z = 0$ midplane. The optical frequency is 320 THz. The deformation is prescribed by Y_1^A and here for clarity of illustration is chosen to be an unreasonably large displacement amplitude producing a relative π phase shift at the APCW output. E_y is normalized to its maximum strength at single-nanobeam input. Here, the number of APCW unit cells is $N = 10$, the total number of taper cells is $N_t = 15$, and the Y-split junction length is $L_Y = 5\ \mu$m.

zero-point motion similar to that for 1D structures with microwave phonons coupled to a photonic defect light mode (50). For comparison of the APCW with 2D structures (as in ref. 53), the mechanical modes are in the few megahertz domain in both cases, but have an effective mass which is two orders of magnitude larger ($\sim$10 ng) for the 2D case.

Beyond traditional perturbation theory which utilizes the unperturbed optical fields to evaluate G_ν^α, a powerful approach to confirm the transduction mechanism consists in solving Maxwell's equations for the propagation of light in the deformed dielectric geometry at all phases of the prescribed mechanical eigenmode. Fig. 7 illustrates this method, where the deformation of the dielectric produces a relative phase shift on the output light relative to the undeformed case. Owing to the large mismatch between optical k_x and acoustic q wavevectors, the deformation is quasi-adiabatic. In particular, for our very long structure and picometer thermal amplitude, radiation losses into nonguided modes are negligible. With this approach we anticipate weaker phase modulation for Y^S, Z^A, and Z^S motions to occur at twice their respective eigenfrequency.

Conclusion and Outlook

We have reported measurements and models that investigate the low-frequency, thermally driven motion of the normal modes of an APCW and the transduction of this motion to the amplitude and phase of weak optical probe beams propagating in a TE guided mode both far from and near to the dielectric band edge of the APCW. The in-plane antisymmetric mode $Y_p^A(x)$ of the two corrugated nanobeam oscillators dominates the optomechanical coupling to TE guided mode light. Simple models describe the basic transduction mechanisms in the waveguide region far from a band edge as well as in a "cavity-like" regime for frequencies near a band edge.

Beyond simple models, full numerical simulations of the APCW structure have been carried out for quantitative predictions of optomechanical coupling G_ν as in Fig. 6. An example is the prospect for detection of zero-point motion $\alpha_{zp}(p = 1) \simeq 14.7$ fm. Following the analysis in ref. 54, we find probe power $\simeq$10 μW would be sufficient to reach phase sensitivity corresponding to α_{zp} for measurement bandwidth equal to the current linewidth $\gamma_1 \sim 24$ Hz for Y_1^A if this mode were cooled to its motional ground state. Moreover, the resulting backaction noise from the probe would correspond to α_{zp}, thereby reaching the standard quantum limit for y motion of the APCW at $f_1 \simeq 2.4$ MHz.

While the quality factors are modest for the APCW compared to current best literature values, the very small effective mass of the APCW allows for thermomechanical force sensitivity at a limit of $\sqrt{S_{FF}} \simeq 143\ \mathrm{aN}/\sqrt{\mathrm{Hz}}$. This value is only $\sim$2.6 times larger than that of ref. 53 ($55\ \mathrm{aN}/\sqrt{\mathrm{Hz}}$), namely $S_{FF} = 4\pi m_{\mathrm{eff}} f_1 k_B T/Q$. However, state-of-the-art engineering of 1D nanobeam resonators with ultrahigh quality factors combined with ultralow effective mass ($\sim$ pg) of localized mechanical modes can reach force sensitivities of a few $\mathrm{aN}/\sqrt{\mathrm{Hz}}$ in the similar frequency range (55).

In terms of cooling to the ground state from a room-temperature APCW, the minimum Q-frequency product $Q \cdot f = 6 \times 10^{12}$ Hz (56) would require Q values about 26 times larger than currently observed. Certainly, many advanced design strategies are available for increasing quality factors for a "next generation" of 1D PCWs (53, 55, 57, 58). In addition, low GM powers lead to strong pondermotive forces within the gap of the APCW that could potentially be harnessed to increase mechanical quality factors by $\sim$50 times by way of "optical springs" (59). Beyond the focus of this article, we can excite selectively the observed mechanical modes with amplitude-modulated guided light at the specific observed frequencies. In fact, we also observe driving of the mechanical resonances with the external optical conveyor belt described in ref. 60.

As for optical cooling of the APCW, our initial measurements related to optomechanics in a nonlinear regime suggest that efficient cooling might be achieved by operating near a band edge. For example, as illustrated by *SI Appendix*, Fig. S5, we observe low-power bistable behavior marked with strong self-oscillation (near radian-phase modulation amplitude) for continuous GM power thresholds below 100 μW. The large-scale oscillations could originate from thermal effects of the APCW due to the GM light, which we are investigating. Alternatively, the bistable behavior and self-induced oscillates might arise from optical spring effects as described in ref. 2. A double-well potential with two stable local minima can be developed when the GM power is sufficiently high (7). The detailed mechanism of the large-scale oscillations is beyond the scope of this paper and will be investigated in our subsequent experiments. Related instabilities for blue cavity detunings are a hallmark of cooling for red detunings in conventional optomechanics in optical cavities (61).

The observations on mechanical modes of the APCW reported here are also important for assessing deleterious heating

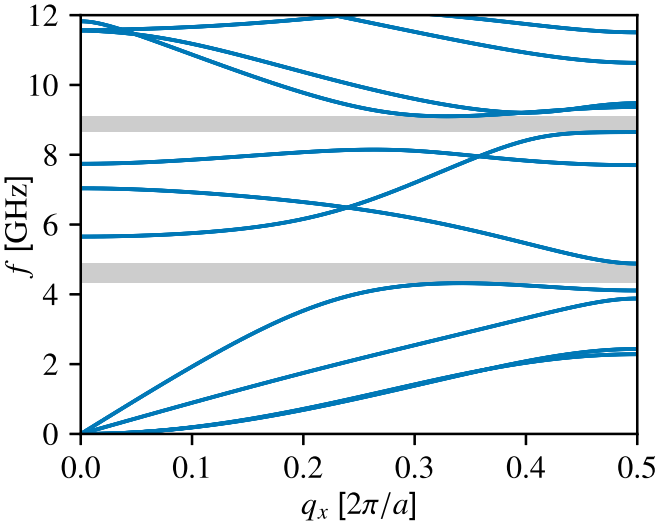

Fig. 8. Phononic band diagram of the infinite APCW structure, with the acoustic wavevector component q_x spanning the irreducible Brillouin zone. The gray-shaded areas represent band gaps, with opportunity for flat bands and band-gap physics with frequencies tuned to the hyperfine ground-state frequency of alkali atoms.

mechanisms for combining atom trapping in the vicinity of nanophotonic structures (62). While the symmetric modes lead to negligible modulations of the guided light as compared to Y^A motion, the guided light intensity distribution still follows the motion of the APCW structure in the laboratory frame. A simple estimate of heating limited trap lifetime due to trap-potential pointing instability can be obtained from the thermal position instability of $\sqrt{S_{yy}} \sim 3.8\,\mathrm{pm}/\sqrt{\mathrm{Hz}}$ at f_1, with $S_{yy} = 2k_B TQ/m_{\mathrm{eff}}\omega_1^3$ (54) corresponding to the maximum displacement of one of the nanobeams (located at the midpoint along x for the fundamental mode; *SI Appendix*, Fig. S8). This noise level corresponds to an energy-doubling time τ (63) of order 1 ms, at atom trap frequency f_1. We are working on further simulations of heating rates with the complex motion of these dielectric structures for cold atom traps. Implementing feedback cooling with guided light could also mitigate limitations from operation at room temperature (64).

Although we have concentrated on low-frequency eigenmodes of the APCW in the megahertz regime, we have also investigated eigenmodes in the gigahertz regime that are of interest for many of the topics addressed here. As illustrated in Fig. 8, the corrugated structure of the APCW can lead to phononic band gaps in the gigahertz acoustic domain. The possibilities for band-gap engineering for both photons and phonons (50) for application to atomic physics (e.g., for coupling mechanics to both Zeeman and hyperfine atomic states) represent an exciting frontier beyond the work reported here. One example to note is that the curvature of phonon bands can strongly enhance heating rates for atom traps (65), which might offer new possibilities for engineering better atom traps in PCWs for atomic physics.

Data Availability. All study data are included in this article and *SI Appendix*.

ACKNOWLEDGMENTS. We acknowledge sustained and important interactions with A. P. Burgers, L. S. Peng, and S.-P. Yu, who fabricated the nanophotonic structures used for this research. J.-B.B. acknowledges enlightening discussions with Y. Tsaturyan. H.J.K. acknowledges funding from the Office of Naval Research (ONR) Grant N00014-16-1-2399, the ONR Multidisciplinary University Research Initiative (MURI) Quantum Opto-Mechanics with Atoms and Nanostructured Diamond Grant N00014-15-1-2761, the Air Force Office of Scientific Research MURI Photonic Quantum Matter Grant FA9550-16-1-0323, and the National Science Foundation Grant PHY-1205729.

1. V. Braginsky, S. Strigin, S. Vyatchanin, Parametric oscillatory instability in Fabry–Perot interferometer. *Phys. Lett. A* **287**, 331–338 (2001).
2. H. Rokhsari, T. J. Kippenberg, T. Carmon, K. J. Vahala, Radiation-pressure-driven micro-mechanical oscillator. *Opt. Express* **13**, 5293–5301 (2005).
3. K. Hammerer, M. Aspelmeyer, E. S. Polzik, P. Zoller, Establishing Einstein-Poldosky-Rosen channels between nanomechanics and atomic ensembles. *Phys. Rev. Lett.* **102**, 020501 (2009).
4. P. Rabl *et al.*, A quantum spin transducer based on nanoelectromechanical resonator arrays. *Nat. Phys.* **6**, 602–608 (2010).
5. P. Rabl *et al.*, Strong magnetic coupling between an electronic spin qubit and a mechanical resonator. *Phys. Rev. B* **79**, 041302 (2009).
6. K. Hammerer *et al.*, Strong coupling of a mechanical oscillator and a single atom. *Phys. Rev. Lett.* **103**, 063005 (2009).
7. M. Aspelmeyer, T. J. Kippenberg, F. Marquardt, Cavity optomechanics. *Rev. Mod. Phys.* **86**, 1391–1452 (2014).
8. A. D. O'Connell *et al.*, Quantum ground state and single-phonon control of a mechanical resonator. *Nature* **464**, 697–703 (2010).
9. J. Chan *et al.*, Laser cooling of a nanomechanical oscillator into its quantum ground state. *Nature* **478**, 89–92 (2011).
10. T. P. Purdy, R. W. Peterson, C. A. Regal, Observation of radiation pressure shot noise on a macroscopic object. *Science* **339**, 801–804 (2013).
11. A. H. Safavi-Naeini *et al.*, Observation of quantum motion of a nanomechanical resonator. *Phys. Rev. Lett.* **108**, 033602 (2012).
12. D. W. C. Brooks *et al.*, Non-classical light generated by quantum-noise-driven cavity optomechanics. *Nature* **488**, 476–480 (2012).
13. A. H. Safavi-Naeini *et al.*, Squeezed light from a silicon micromechanical resonator. *Nature* **500**, 185–189 (2013).
14. T. P. Purdy, P. L. Yu, R. W. Peterson, N. S. Kampel, C. A. Regal, Strong optomechanical squeezing of light. *Phys. Rev. X* **3**, 031012 (2013).
15. J. D. Teufel *et al.*, Sideband cooling of micromechanical motion to the quantum ground state. *Nature* **475**, 359–363 (2011).
16. T. A. Palomaki, J. D. Teufel, R. W. Simmonds, K. W. Lehnert, Entangling mechanical motion with microwave fields. *Science* **342**, 710–713 (2013).
17. D. Rugar, R. Budakian, H. J. Mamin, B. W. Chui, Single spin detection by magnetic resonance force microscopy. *Nature* **430**, 329–332 (2004).
18. S. Hong *et al.*, Coherent, mechanical control of a single electronic spin. *Nano Lett.* **12**, 3920–3924 (2012).
19. S. Kolkowitz *et al.*, Coherent sensing of a mechanical resonator with a single-spin qubit. *Science* **335**, 1603–1606 (2012).
20. O. Arcizet *et al.*, A single nitrogen-vacancy defect coupled to a nanomechanical oscillator. *Nat. Phys.* **7**, 879–883 (2011).
21. E. R. MacQuarrie, T. A. Gosavi, N. R. Jungwirth, S. A. Bhave, G. D. Fuchs, Mechanical spin control of nitrogen-vacancy centers in diamond. *Phys. Rev. Lett.* **111**, 227602 (2013).
22. J. Teissier, A. Barfuss, P. Appel, E. Neu, P. Maletinsky, Strain coupling of a nitrogen-vacancy center spin to a diamond mechanical oscillator. *Phys. Rev. Lett.* **113**, 020503 (2014).
23. P. Ovartchaiyapong, K. W. Lee, B. A. Myers, A. C. B. Jayich, Dynamic strain-mediated coupling of a single diamond spin to a mechanical resonator. *Nat. Commun.* **5**, 4429 (2014).
24. D. Chang, J. Douglas, A. González-Tudela, C. L. Hung, H. Kimble, Colloquium: Quantum matter built from nanoscopic lattices of atoms and photons. *Rev. Mod. Phys.* **90**, 031002 (2018).
25. P. Lodahl *et al.*, Chiral quantum optics. *Nature* **541**, 473–480 (2017).
26. S. P. Yu *et al.*, Nanowire photonic crystal waveguides for single-atom trapping and strong light-matter interactions. *Appl. Phys. Lett.* **104**, 111103 (2014).
27. J. D. Hood *et al.*, Atom–atom interactions around the band edge of a photonic crystal waveguide. *Proc. Natl. Acad. Sci. U.S.A.* **113**, 10507–10512 (2016).
28. S. P. Yu, "Nano-photonic platform for atom-light interaction," PhD thesis, California Institute of Technology, Pasadena, CA (2017).
29. A. C. McClung, "Photonic crystal waveguides for integration into an atomic physics experiment," PhD thesis, California Institute of Technology, Pasadena, CA (2017).
30. J. D. Hood, "Atom-light interactions in a photonic crystal waveguide," PhD thesis, California Institute of Technology, Pasadena, CA, (2017).
31. M. T. Manzoni, L. Mathey, D. E. Chang, Designing exotic many-body states of atomic spin and motion in photonic crystals. *Nat. Commun.* **8**, 14696 (2017).
32. D. E. Chang, K. Sinha, J. M. Taylor, H. J. Kimble, Trapping atoms using nanoscale quantum vacuum forces. *Nat. Commun.* **5**, 4343 (2013).
33. R. Blatt, D. Wineland, Entangled states of trapped atomic ions. *Nature* **453**, 1008–1015 (2008).
34. H. Haffner, C. F. Roos, R. Blatt, Quantum computing with trapped ions. *Phys. Rep.* **469**, 155–203 (2008).
35. L. M. Duan, C. Monroe, Colloquium: Quantum networks with trapped ions. *Rev. Mod. Phys.* **82**, 1209–1224 (2010).
36. A. Reiserer, G. Rempe, Cavity-based quantum networks with single atoms and optical photons. *Rev. Mod. Phys.* **87**, 1379–1418 (2015).
37. R. M. Shelby, M. D. Levenson, P. W. Bayer, Guided acoustic-wave Brillouin scattering. *Phys. Rev. B* **31**, 5244–5252 (1985).
38. R. M. Shelby, M. D. Levenson, P. W. Bayer, Resolved forward Brillouin scattering in optical fibers. *Phys. Rev. Lett.* **54**, 939–942 (1985).
39. J. B. Béguin *et al.*, Advanced apparatus for the integration of nanophotonics and cold atoms. *Optica* **7**, 1–2 (2020).
40. X. Luan *et al.*, The integration of photonic crystal waveguides with atom arrays in optical tweezers. *Adv. Quantum Technol.*, **3**, 2000008 (2020).
41. F. Hocke *et al.*, Determination of effective mechanical properties of a double-layer beam by means of a nano-electromechanical transducer. *Appl. Phys. Lett.* **105**, 133102 (2014).
42. H. O. Pierson, *Handbook of Chemical Vapor Deposition (CVD): Principles, Technology, and Applications* (Elsevier, 1999).
43. R. Leijssen, G. R. L. Gala, L. Freisem, J. T. Muhonen, E. Verhagen, Nonlinear cavity optomechanics with nanomechanical thermal fluctuations. *Nat. Commun.* **8**, ncomms16024 (2017).
44. S. A. Fedorov *et al.*, Thermal intermodulation noise in cavity-based measurements. arXiv:2004.05700 (14 May 2020).
45. R. Zhang *et al.*, High mechanical $f_m q_m$product tuning fork cavity optomechanical transducers. *Adv. Photon.* **7**, 5600 (2015).
46. M. Eichenfield, R. Camacho, J. Chan, K. J. Vahala, O. Painter, A picogram- and nanometre-scale photonic-crystal optomechanical cavity. *Nature* **459**, 550–555 (2009).
47. S. G. Johnson *et al.*, Perturbation theory for Maxwell's equations with shifting material boundaries. *Phys. Rev. E* **65**, 066611 (2002).
48. M. Eichenfield, J. Chan, A. H. Safavi-Naeini, K. J. Vahala, O. Painter, Modeling dispersive coupling and losses of localized optical and mechanical modes in optomechanical crystals. *Opt. Express* **17**, 20078–20098 (2009).
49. F. Gyger *et al.*, Observation of stimulated Brillouin scattering in silicon nitride integrated waveguides. *Phys. Rev. Lett.* **124**, 013902 (2020).
50. M. Eichenfield, J. Chan, R. M. Camacho, K. J. Vahala, O. Painter, Optomechanical crystals. *Nature* **462**, 78–82 (2009).
51. M. J. Burek *et al.*, Diamond optomechanical crystals. *Optica* **3**, 1404 (2016).
52. Y. Li *et al.*, Optomechanical crystal nanobeam cavity with high optomechanical coupling rate. *J. Optic.* **17**, 045001 (2015).

53. Y. Tsaturyan, A. Barg, E. S. Polzik, A. Schliesser, Ultracoherent nanomechanical resonators via soft clamping and dissipation dilution. *Nat. Nanotechnol.* **12**, 776–783 (2017).
54. A. A. Clerk, M. H. Devoret, S. M. Girvin, F. Marquardt, R. J. Schoelkopf, Introduction to quantum noise, measurement, and amplification. *Rev. Mod. Phys.* **82**, 1155–1208 (2010).
55. A. H. Ghadimi *et al.*, Elastic strain engineering for ultralow mechanical dissipation. *Science* **360**, 764–768 (2018).
56. D. J. Wilson, C. A. Regal, S. B. Papp, H. J. Kimble, Cavity optomechanics with stoichiometric SiN films. *Phys. Rev. Lett.* **103**, 207204 (2009).
57. C. Reinhardt, T. Müller, A. Bourassa, J. C. Sankey, Ultralow-noise SiN trampoline resonators for sensing and optomechanics. *Phys. Rev. X* **6**, 021001 (2016).
58. C. Reetz *et al.*, Analysis of membrane phononic crystals with wide band gaps and low-mass defects. *Phys. Rev. Appl.* **12**, 044027 (2019).
59. K. K. Ni *et al.*, Enhancement of mechanical q factors by optical trapping. *Phys. Rev. Lett.* **108**, 214302 (2012).
60. A. P. Burgers *et al.*, Clocked atom delivery to a photonic crystal waveguide. *Proc. Natl. Acad. Sci. U.S.A.* **116**, 456–465 (2019).
61. T. J. Kippenberg, K. J. Vahala, Cavity opto-mechanics. *Opt. Express* **15**, 17172 (2007).
62. H. Zoubi, K. Hammerer, Optomechanical multimode Hamiltonian for nanophotonic waveguides. *Phys. Rev. A* **94**, 053827 (2016).
63. T. A. Savard, K. M. O'Hara, J. E. Thomas, Laser-noise-induced heating in far-off resonance optical traps. *Phys. Rev. A* **56**, R1095–R1098 (1997).
64. O. Arcizet, P. F. Cohadon, T. Briant, M. Pinard, A. Heidmann, Radiation-pressure cooling and optomechanical instability of a micromirror. *Nature* **444**, 71–74 (2006).
65. D. Hümmer, P. Schneeweiss, A. Rauschenbeutel, O. Romero-Isart, Heating in nanophotonic traps for cold atoms. *Phys. Rev. X* **9**, 041034 (2019).